

## Research paper

# Permeability and frictional properties of halite–clay–quartz faults in marine-sediment: The role of compaction and shear



Bryan M. Kaproth <sup>a, b</sup>, Marek Kacwicz <sup>c</sup>, Sankar Muhuri <sup>c</sup>, Chris Marone <sup>a, \*</sup>

<sup>a</sup> Department of Geosciences, and Energy Institute Center for Geomechanics, Geofluids, and Geohazards, The Pennsylvania State University, University Park, PA, USA

<sup>b</sup> Noble Energy Corporation, Denver, CO, USA

<sup>c</sup> Chevron Corporation, Houston, TX, USA

## ARTICLE INFO

## Article history:

Received 23 April 2016

Received in revised form

22 August 2016

Accepted 14 September 2016

Available online 15 September 2016

## Keywords:

Faulting

Permeability

Fault seal

Friction

## ABSTRACT

Faults in marine-sediment basins often dictate fluid flow and act as petroleum traps or seals. Permeability contrasts between these zones and the surrounding country rock can be large, depending on fault composition, stress, and strain history. Despite the importance of such faults, our understanding of their frictional properties and permeability is relatively poor. Here we report on a suite of laboratory experiments to assess the roles of fault composition, stress, and shear strain for dictating poromechanical properties of fault. Experiments were conducted at room temperature on synthetic fault gouge composed of quartz, halite, and clay (illite shale or Ca-montmorillonite). We sheared layers that were 5–7 mm thick and measured fault permeability at effective normal stresses from 2 to 6 MPa for hydrostatic conditions and after shear strains from 2 to 10. We find that fault permeability is highly sensitive to clay content, with permeabilities spanning 2–4 orders of magnitude under otherwise identical conditions. Permeability decreased up to 2 orders of magnitude with imposed shear strain >1 and ~1 order of magnitude with increasing normal stress from 2 to 6 MPa. During shear, halite deformed via both ductile flow and brittle failure, while quartz and clay particles formed force chains that spanned the layers and defined shear localization fabrics. Samples with higher halite content exhibited greater permeability reduction, perhaps by plastic flow and pressure solution. Our results suggest that the permeability of faults in marine sediment is dictated by clay content, and that the most dramatic permeability changes occur with relatively small fault throw (shear strain from 2 to 5). This highlights the importance of understanding minor faults and fault sets when estimating subsurface fluid flow and potential reservoir compartmentalization.

© 2016 Elsevier Ltd. All rights reserved.

## 1. Introduction

Faults represent significant geologic features for subsurface fluid flow and are important in numerous transport processes within sedimentary basins where they affect petroleum reservoir quality, hydrocarbon migration, and groundwater flow (Smith, 1966; Aydin and Johnson, 1983; López and Smith, 1995; Evans et al., 1997; Aydin, 2000; Kim et al., 2004; Baud et al., 2004). Fault permeability and poromechanical properties can impact deformation style in reservoir rocks and a variety of tectonic environments (e.g., Arch and Maltman, 1990; Caine et al., 1996; Caine and Forster, 1999;

Crawford, 1998; Zhang et al., 1999; Fisher et al., 2001; Chuhan et al., 2003; Wibberley and Shimamoto, 2003; Odling et al., 2004; Mitchell and Faulkner, 2008, 2012; Ikari et al., 2009a,b; Balsamo and Storti, 2010; Faulkner et al., 2010; Foroozan et al., 2012; Carruthers et al., 2013; Gomila et al., 2016). In particular, faults can act as fluid conduits in impermeable environments (e.g., shales, granites, basalts, etc.), fluid barriers in permeable environments (e.g., sandstones), and they may act to redirect flow in cases where faults develop significant permeability anisotropy (Knipe, 1992; Evans et al., 1997; Fisher and Knipe, 1998, 2001; Zhang and Tullis, 1998; Bos and Spiers, 2000; Shipton et al., 2005; Benson et al., 2006; Fossen and Bale, 2007; Takahashi et al., 2007; Daniel and Kaldi, 2008; Crawford et al., 2008; De Paola et al., 2009; Faulkner et al., 2010; Savage and Brodsky, 2011; Ballas et al., 2012; Ikari and Saffer, 2012; Faoro et al., 2012, 2013; Olierook et al., 2014;

\* Corresponding author.

E-mail address: [cjm38@psu.edu](mailto:cjm38@psu.edu) (C. Marone).

Scuderi et al., 2015; Seebeck et al., 2015).

Fault permeability can be significantly lower than the wall rock, especially in marine sediment environments where clay is integrated into fault zones (Caine et al., 1996; Evans et al., 1997; Gibson, 1998; Crawford et al., 2008; Ikari et al., 2009a; Faulkner et al., 2010; Ishibashi et al., 2012; Mitchell and Faulkner, 2012; Harding and Huuse, 2015). In these environments, faults juxtapose and mix clays from shale along with sands and silts from other horizons (e.g., Bjørlykke and Høeg, 1997; Billi et al., 2003; Faulkner et al., 2010). Important processes include abrasional mixing, clay smearing, and pore throat clogging. Fault permeability is often dictated by pore conduit connectivity or narrow crack apertures, depending on mineralogy and development of shear fabric (Revil et al., 2002; Takahashi et al., 2007; Crawford et al., 2008; Ikari et al., 2009b; Niemeijer et al., 2010; Cheung et al., 2012; Scuderi et al., 2015). Indeed, small increases in clay concentrations can dramatically reduce fault permeability in sandy faults (Revil et al., 2002; Crawford et al., 2008; Faulkner et al., 2010). For example, Crawford et al. observed a four order of magnitude permeability reduction as clay content increased from 0 to 50% under otherwise identical conditions. While much work has been done to quantify the roles of clay content, load, and strain on fault permeability (e.g., Bentley and Barry, 1991; Antonellini and Aydin, 1994; Revil et al., 2002; Lothe et al., 2002; Wibberley and Shimamoto, 2003; Sternlof et al., 2004; Fortin et al., 2005; Crawford et al., 2008; Mondol et al., 2008; Tueckmantel et al., 2010; Ballas et al., 2012; Skurtveit, 2013; Scuderi et al., 2015), our understanding of the relationship between fault strength and permeability remains relatively poor.

Here, we focus on complex mixtures of synthetic fault gouge to illuminate the role of shear, fabric development and ductile flow, with application to faults found in association with salt domes and surrounding country rock. One goal of this work is to provide input for geomechanical models of salt bodies, which require information on both permeability and friction constitutive properties of the salt-clay-sediment mixtures that often bound them.

Impermeable salt domes (Peach and Spiers, 1996) often have associated faults, and these features can act in concert to seal reservoirs (Jackson et al., 1994; Rowan et al., 1999; Hudec and Jackson, 2007; Fort and Brun, 2012). In these cases, the fault zones often integrate halite from the salt dome as well as nearby salt layers. Halite undergoes a range of deformation behaviors depending on the chemistry, composition, materials it mixes with, stress, and strain history on the fault, and thus its role for fault zone permeability is complex. Under fast slip conditions halite tends to deform brittlely (e.g., Shimamoto, 1986; Bos et al., 2000a,b; Niemeijer et al., 2010; Wong and Baud, 2012) and should behave as a framework grain. During slower deformation and for transient slip, halite likely accommodates shear via a combination of brittle and ductile deformation and/or pressure solution (Rutter, 1983; Shimamoto, 1986; Bos et al., 2000a,b; Niemeijer et al., 2008, 2010).

The purpose of this paper is to present results from a comprehensive laboratory study of the permeability and frictional properties of marine-sediment faults as a function of composition, stress, and shear strain. We studied synthetic faults composed of quartz, halite, and illite shale or smectite clay. We report on frictional properties and fault-normal permeability as a function of strain and effective normal stress, focusing primarily on low effective stress (<6 MPa) relevant for overpressured environments.

## 2. Methods and materials

We measured permeability and frictional properties of simulated fault zones as a function of normal stress and shear strain. We conducted experiments in the double-direct shear configuration

under true triaxial stress conditions (e.g., Ikari et al., 2009a; Samuelson et al., 2009; Kaproth and Marone, 2014; Carpenter et al., 2015). The experimental geometry is shown in Fig. 1. To simulate faults in marine-sediment basins we conducted experiments on mixtures of quartz sand, illite shale or smectite clay (Ca-montmorillonite), and halite (Table 1 and Fig. 2). Our sample compositions were designed to span the transition between clast-supported and matrix supported fault gouge, where fault zone porosity is lowest and permeability changes are strongest (e.g., Faulkner et al., 2010). We used commercial silt-sized quartz foundry sand (F110) and Ca-montmorillonite (sieved to <125  $\mu\text{m}$ ). Illite shale and pure halite were ground in a rotary mill and sieved to <125  $\mu\text{m}$ . The illite shale is primarily illite with some quartz, plagioclase, and minor kaolinite (Ikari et al., 2009a). Our experiments were carried out under conditions where pressure solution and ductile deformation of halite is operative at low strain rates and during holds, but halite and the other minerals deform via brittle deformation for the shearing rates used (e.g., shear displacement rate of 10  $\mu\text{m/s}$  or shear strain rate of  $\sim 2 \times 10^{-3} \text{ s}^{-1}$ ). Our pore fluid was a saturated NaCl brine, 35.7 g/ml, obtained by adding pure NaCl to deionized water. We ensured NaCl saturation by regularly adding salt grains to the brine bath.

We deformed synthetic faults as layers in the double direct shear configuration under constant effective stress normal to the layers (Fig. 2). In this configuration, two identical layers of fault-gouge are sandwiched between three forcing blocks (Fig. 1). All stresses, displacements, and other measurements reported here are given for one layer of the double direct shear geometry. Shear displacement at the fault boundary is imposed by driving the central block with a hydraulic ram, inducing shear within the fault gouge layers. We arranged the true triaxial apparatus for constant confining pressure, with normal stress and shear stress applied to the sample directly via hydraulic pistons (Fig. 1). All stresses and fluid flow rates were maintained by fast-acting, servo-hydraulic control. Strain gauge load cells, accurate to  $\pm 0.1$  kPa, measured applied stresses. Direct current displacement transducers (DCDTs), accurate to  $\pm 0.1$   $\mu\text{m}$ , measured shear and normal displacement on the faults. Pressure transducers, accurate to  $\pm 7$  kPa, measured the confining and pore pressure. Stresses, pressures, and displacements were digitally recorded at 10 kHz with a 24 bit system, and were averaged to 10–100 Hz for storage.

Fault layers were constructed to specific initial thicknesses from 5 to 7 mm. To ensure reproducibility of the tests we weighed the sample material used to construct each layer. Layer thickness was measured carefully on the bench during sample construction and then again in the testing machine once a small normal load was applied. These measurements were accurate to  $\pm 50$   $\mu\text{m}$ . Layer thickness was also measured at the end of the run, prior to unloading, which allowed us to check and verify the thickness and thickness change compared to that measured via the DCDT. We calculated average shear strain  $\gamma$  within the layer as the sum of  $dx/h$ , where  $dx$  is a given shear displacement increment (normally <1  $\mu\text{m}$  for our digital sampling rates) and  $h$  is the measured layer thickness, which is updated continuously during shear.

Porous steel frits act as the interface between the steel forcing blocks and the sample layers, distributing the pore pressure and allowing linear flow across the sample (parallel to  $\sigma_n$ ; Fig. 1C). The sample assemblies were sealed with flexible latex jackets to isolate the sample from the confining oil (Fig. 1D). Pore pressures were applied to the sample through the forcing blocks, with upstream pressure ( $P_pA$ ) applied through the center block to both sample layers and downstream pressure ( $P_pB$ ) applied simultaneously to the two side blocks of the double direct shear configuration (Kaproth and Marone, 2014).

Fig. 3 shows representative shear stress curves for three

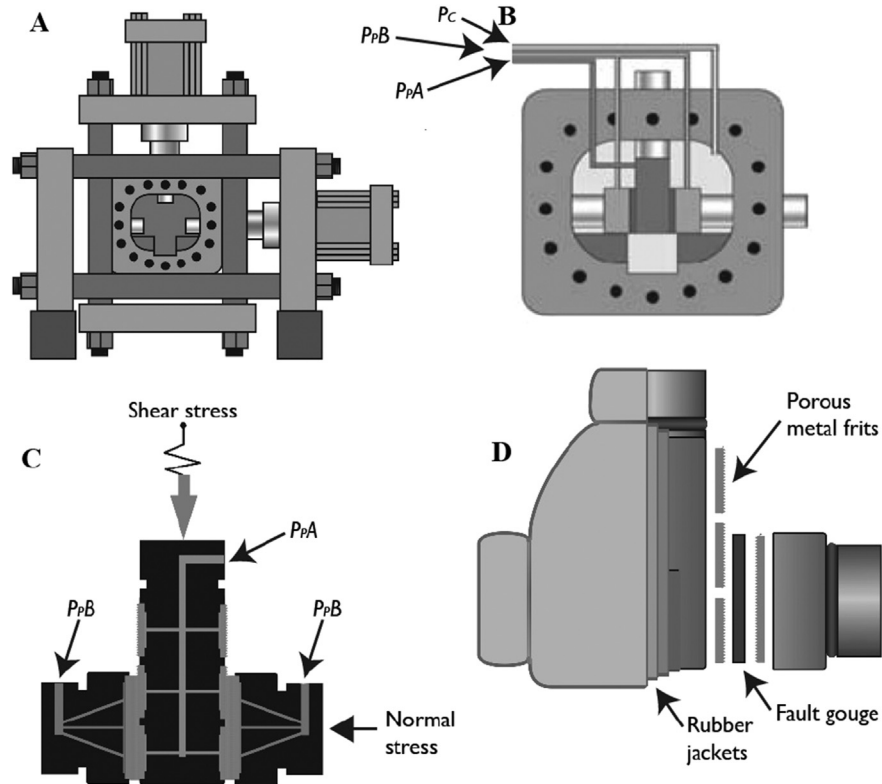


**Fig. 1.** Deformation apparatus and experiment setup. Experiments were conducted in a (A) biaxial apparatus with a (B) true triaxial pressure vessel using the (C) double direct shear assembly. Confining pressure,  $P_c$ , pore pressure inflow,  $P_{pA}$ , and pore pressure outflow,  $P_{pB}$  were applied through steel lines to the sample blocks. (C) Fault gouge was deformed in layers. Normal stress was applied horizontally across both sample layers, and shear stress was applied vertically to the center block, inducing shear within the sample layers. Pore fluid access was via channels and porous metal frits in the side blocks (D). The sample and pore pressures are isolated from the confining pressure with latex rubber jackets.

**Table 1**  
Permeability measurements for all experiments.

Experiment	Quartz/Clay/Halite	Clay type	2 MPa $\sigma'_n$ , 0 $\gamma$		4 MPa $\sigma'_n$ , 0 $\gamma$		6 MPa $\sigma'_n$ , 0 $\gamma$		$\gamma$	6 MPa $\sigma'_n$		$\gamma$	6 MPa $\sigma'_n$	
			$k$ min, m <sup>2</sup>	$k$ max, m <sup>2</sup>	$k$ min, m <sup>2</sup>	$k$ max, m <sup>2</sup>	$k$ min, m <sup>2</sup>	$k$ max, m <sup>2</sup>		$k$ min, m <sup>2</sup>	$k$ max, m <sup>2</sup>		$k$ min, m <sup>2</sup>	$k$ max, m <sup>2</sup>
p3979	100/0/0%	Smectite	2.00E-14	2.00E-14	2.00E-14	2.00E-14	2.00E-14	2.00E-14	2.58	2.00E-14	2.00E-14	6.14	2.00E-14	2.00E-14
p3908	75/12/12	Smectite	1.31E-15	1.68E-15	6.37E-16	1.76E-15	6.37E-16	7.09E-16	1.75	6.25E-17	8.23E-17	5.05	5.74E-17	7.17E-17
p3976	66/17/17	Smectite	4.28E-15	8.28E-15	2.59E-15	3.28E-15	2.19E-15	3.76E-15	2.16	2.11E-16	2.59E-16	5.98	1.80E-16	2.25E-16
p3911	64/24/12	Smectite	3.35E-15	5.01E-15	4.78E-16	7.89E-16	4.31E-16	6.24E-16	3.71	5.47E-17	1.00E-16	9.31	6.31E-17	1.03E-16
p3910	57/21/21	Smectite	2.71E-16	4.42E-16	2.00E-16	2.89E-16	1.86E-16	2.76E-16	2.69	1.33E-17	2.07E-17	7.69	3.45E-17	5.38E-17
p3909	33/33/33	Smectite	1.01E-16	1.40E-16	1.38E-16	2.04E-16	4.80E-17	5.86E-17	3.70	2.72E-18	4.53E-18	11.4	7.67E-18	9.84E-18
p3821	33/54/12	Smectite	2.60E-16	4.30E-16	5.80E-17	7.00E-17	6.20E-17	8.40E-17	3.60	5.10E-19	6.50E-19	8.33	3.90E-18	7.10E-18
p3978	0/50/50	Smectite	5.15E-16	6.96E-16	2.73E-16	4.94E-16	1.57E-16	4.04E-16	4.40	3.40E-18	1.10E-17	10.2	7.37E-18	2.45E-17
p3686*	75/12/12	Illite	3.36E-15	3.64E-15	3.00E-15	4.17E-15	2.75E-15	3.27E-15	2.42	1.47E-15	1.57E-15	5.89	6.05E-16	6.75E-16
p3650*	64/12/24	Illite	9.75E-16	9.06E-16	5.61E-16	5.87E-16	3.61E-16	4.00E-16	2.23	1.43E-16	1.59E-16	5.86	1.58E-16	1.76E-16
p3649*	64/24/12	Illite	9.92E-16	1.95E-15	6.53E-16	9.65E-16	3.23E-16	4.28E-16	1.83	3.29E-17	5.12E-17	5.17	1.90E-17	2.15E-17
p3648*	57/21/21	Illite	2.27E-15	2.65E-15	5.31E-16	7.54E-16	7.57E-16	1.26E-15	1.80	3.17E-16	3.92E-16	5.34	1.05E-16	1.39E-16
p3912	57/21/21	Illite	1.40E-16	2.26E-16	1.36E-16	2.26E-16	1.17E-16	1.53E-16	2.33	2.05E-17	3.93E-17	6.43	3.89E-17	5.57E-17
p3913	33/12/54	Illite	5.26E-16	9.71E-16	1.53E-16	1.85E-16	8.12E-17	1.05E-16	2.17	4.01E-17	5.17E-17	7.03	3.23E-17	3.74E-17
p3822	33/12/54	Illite	1.31E-15	1.68E-15	6.37E-16	1.76E-15	6.37E-16	7.09E-16	1.75	6.25E-17	8.23E-17	5.05	5.74E-17	7.17E-17
p3647*	33/33/33	Illite	1.29E-15	1.57E-15	1.05E-16	1.65E-16	6.13E-17	6.97E-17	2.00	2.33E-18	4.06E-18	6.15	6.26E-18	7.77E-18
p3684*	33/54/12	Illite	4.32E-17	7.37E-17	1.41E-17	1.86E-17	9.17E-18	1.11E-17	2.28	3.02E-18	4.08E-18	5.80	2.54E-18	3.19E-18
p3914	5/5/90	Illite	5.35E-16	1.38E-16	9.21E-17	1.25E-16	7.83E-17	1.34E-16	2.71	5.04E-17	8.40E-17	8.57	8.37E-17	9.83E-17

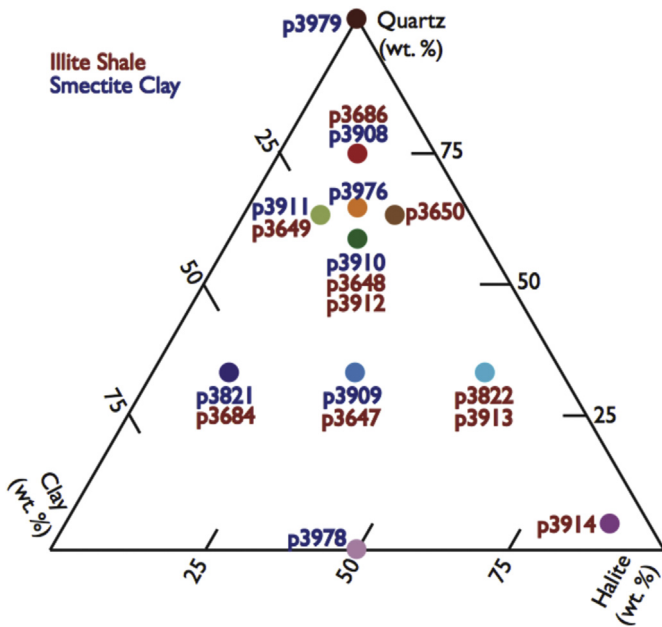


**Fig. 2.** Ternary diagram showing the fault gouge compositions used in this study. Experiments were carried out on mixtures of quartz, halite, and clay (illite shale or montmorillonite). A total of 18 experiments were conducted. Symbol color and experiment number (e.g., p3979 is 100% Qtz) denote mixture composition here and in subsequent figures. (For interpretation of the references to colour in this figure legend, the reader is referred to the web version of this article.)

experiments. Upstream and downstream pore pressures ( $P_{pA}$  and  $P_{pB}$ , respectively) were used to drive saturated NaCl brine through the sample parallel to  $\sigma_n$  and perpendicular to the shear direction (Fig. 1).

We used a standard experimental protocol for all experiments (Table 1). The sample assemblies were loaded into the vessel and a small initial normal load was applied (0.6 MPa  $\sigma_n$ ). At this point layer thickness was measured under load with calipers, and additional thickness changes were tracked with the DCDTs. The initial layer thickness is known to  $\pm 50 \mu\text{m}$ , and changes in layer thickness are measured to  $\pm 0.1 \mu\text{m}$ . The pressure vessel was then filled with oil, and a small confining pressure was applied (0.35 MPa). To saturate the sample initially we removed air from the sample by pulling a vacuum from  $P_{pB}$ . After the vacuum was drawn down to the lowest point for  $\sim 1$  min, pore fluid was introduced through  $P_{pA}$  at a low constant flow rate. Flow was maintained until the effluent was free of air for  $\sim 20$  min ( $\sim 40$  min total). After initial saturation,  $\sigma_n'$  was increased to 2, 4, and 6 MPa with a permeability test at each load (see Table 2 for descriptions of  $\sigma_n$ , pore pressure, and confining pressure histories). For the double direct shear configuration in the true triaxial apparatus effective normal stress on the layers is given as:  $\sigma_n' = \sigma_n - P_p + 0.5P_c$ , where  $P_p$  is the average pore pressure,  $P_c$  is the confining pressure, and the term  $0.5P_c$  represents the affect of confining pressure on normal load due to the sample geometry (e.g., Samuelson et al., 2009; Kaproth and Marone, 2014).

Fig. 4 shows the time history for our standard loading procedure for a representative experiment. Fluid was driven through the sample by applying a constant upstream pressure  $P_{pA}$  and a constant flow rate  $Q$  into the downstream fluid reservoir  $P_{pB}$  (Fig. 1). Thus, flow occurs from the center block of the double direct shear (DDS) configuration to the side blocks where it is collected and measured as the total flow through both layers. We determined permeability following Darcy's Law,  $k = Q\eta h / (A \Delta P_p)$ , where  $Q$  is the volumetric flow rate,  $\eta$  is the fluid viscosity,  $h$  is the layer thickness, (we use the actual value of  $h$  which is measured continuously with

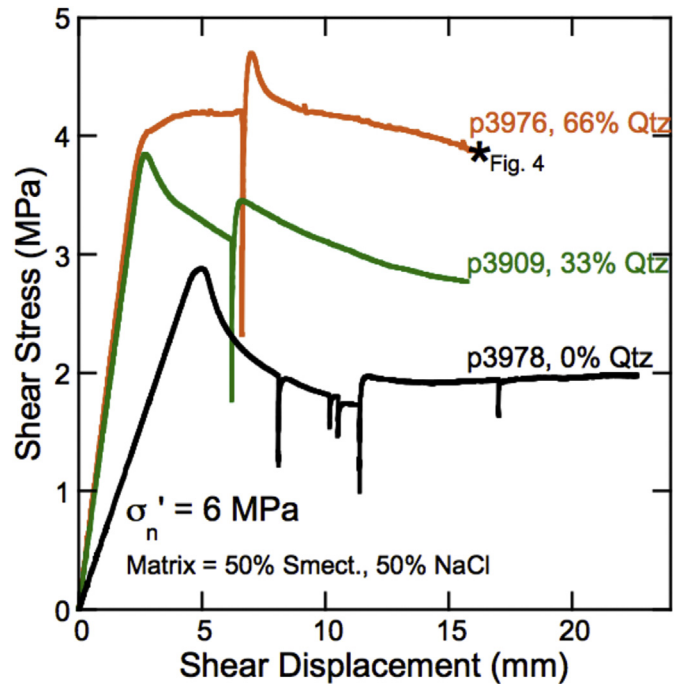


**Fig. 3.** Friction curves from three representative experiments. See Fig. 2 for composition details. Each curve shows a stage of elastic loading followed by the onset of plastic strain and shear deformation. After peak stress materials with high clay content weaken dramatically, and for the sample with no quartz the coefficient of residual sliding friction ( $\mu$ ) is  $\sim 0.3$ . Vertical line segments after 5 mm of shear displacement represent 'hold' periods designed to measure frictional restrengthening and permeability. Frictional strength increases with increasing quartz content; maximum residual friction values for steady sliding are 0.6–0.7, which is typical for a clast-supported mixture. In each experiment shear was stopped (hold periods) during permeability tests and then resumed, resulting in a drop in shear stress followed by a large peak that represents sample lithification and frictional healing. Several hold tests were done in experiment p3978.

the DCDT),  $A$  is the sample contact area ( $\sim 0.005 \text{ m}^2$ ), and  $\Delta P_p = (P_{pA} - P_{pB})$  is the pressure difference across the sample layers. All of our measurements are referenced to one layer, including  $h$ ,  $A$ , and  $Q$ . Fig. 5 shows the full details of a representative permeability test. Uncertainty in our permeability measurements (e.g., Fig. 5; Table 1) was determined from the measured flow rate and fluid pressure, accounting for specific storage effects as well as variations in flow rate and pressure.

Fig. 6 shows linear flow rates ( $q$ ) and the differential pressures during each of the five permeability tests in p3911, where  $q = Q/A$ . To limit dissolution, we generally used very low constant flow rates ( $q < 50 \mu\text{m/s}$ ) and flow volumes, and pore fluid was typically flowed in and out of the sample (e.g., Fig. 4, sawtooth pattern). These steps limited new pore water interaction with the sample. In some of the early experiments, permeability tests were carried out under constant pressure conditions, which generally required larger pressure differences and flow rates, and may have caused minor halite dissolution, despite the fact that the pore fluid was a brine saturated with NaCl.

**Table 2**  
Load steps for each experiment.

$\sigma_n'$	$\sigma_n$	$P_c$	$P_p$
6	4.5	3	2.4
4	3.0	2	1.6
2	1.5	1	0.8
0.5	0.6	0.35	0

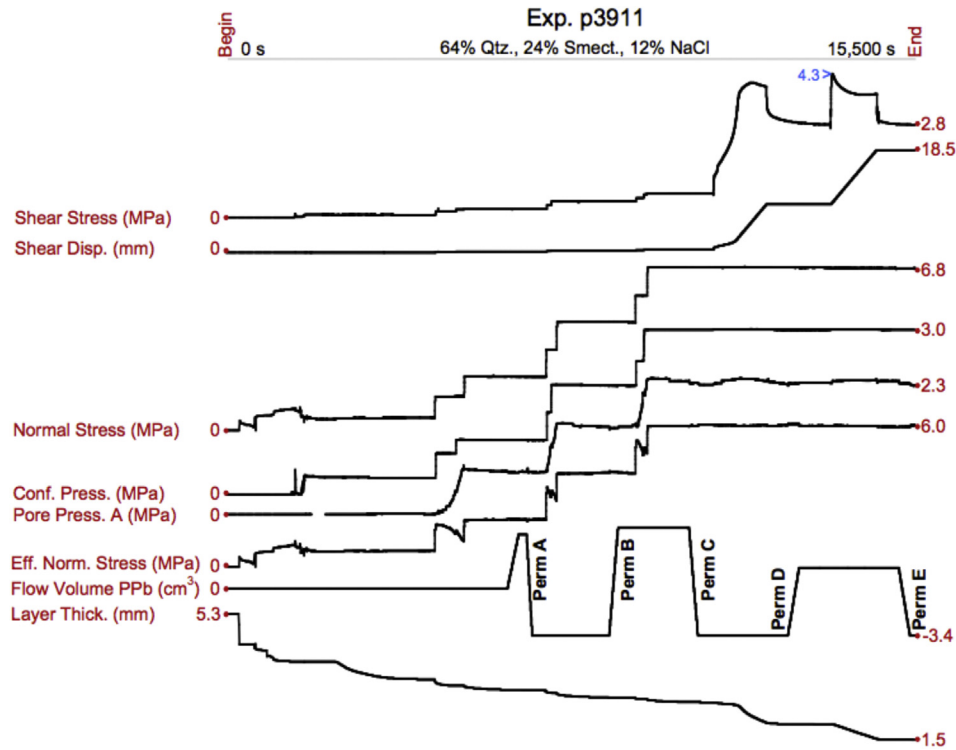


**Fig. 4.** Complete history for a representative experiment. Each line is noted with the initial and final values, for example shear stress starts at 0 and ends at 2.8 MPa, after 15,500 s. The y axis for each line is linear. Normal stress is applied initially to 0.6 MPa and then confining pressure is applied followed by pore pressure. Note history of effective normal stress  $\sigma_n'$  shown below Pore Pressure A in the upstream reservoir (Fig. 1). After 1 h of initial fluid saturation, samples were loaded to 2 MPa  $\sigma_n'$  through a combination of increased pore pressure,  $\sigma_n$ , and confining pressure,  $P_c$ . A permeability test (i.e. Perm. A) was conducted at constant flow rate after the sample reached steady-state compaction. Following the perm test, the sample was loaded to 4, and 6 MPa, and then the sample was sheared. Each of these steps preceded a permeability test.

At 6 MPa  $\sigma_n'$  each sample was sheared 10 mm, after which a  $k$  test was conducted (Fig. 3). Initial shear was corrected for the elasticity of the latex jacket following standard procedure (Samuelson et al., 2009; Ikari et al., 2009a), accommodating ~ 5 mm of the initial vertical displacement. Each sample was again sheared 10 mm and the final  $k$  test was conducted. Fig. 6 shows permeability tests at 2, 4, and 6 MPa  $\sigma_n'$  with zero strain, and at low and high strain at 6 MPa  $\sigma_n'$  (i.e. Perm. A – E) for a representative experiment. Under each of these conditions and prior to each  $k$  test, the sample was allowed to compact until compaction rates were less than 0.04  $\mu\text{m/s}$  (Fig. 4), limiting permeability transients.

**3. Results**

Our fault zones exhibited permeabilities from  $>2 \times 10^{-14}$  to  $\sim 3 \times 10^{-19} \text{ m}^2$ , which is within the range of capability for our testing machine (Ikari et al., 2009a; Samuelson et al., 2009). Fig. 6b shows the permeability history for p3911, with permeabilities ranging from  $\sim 4 \times 10^{-15}$  to  $\sim 8 \times 10^{-17} \text{ m}^2$ . Fig. 7 shows permeability as a function of load and strain for smectite experiments, and Fig. 8 shows permeability for illite bearing experiments. The highest permeabilities occurred for pure quartz sand at low stresses, exceeding the capabilities of our system in some cases.

In general, permeability decreased as a function of decreasing quartz content and increasing matrix content (e.g., clay and halite). Fig. 9 shows permeability contours interpolated between a number of our experiments, prior to and after the application of shear strain. From 75% to 33% quartz content the permeability decreased by ~1–2 orders of magnitude with shear strain. In both the smectite and illite samples, the lowest permeabilities occur for mixtures of

33/54/12% by mass quartz/clay/halite, closely followed by the 33/33/33% mixtures. Superimposed on these values are trends of permeability decrease with load and strain (Fig. 9).

We found that permeability decreased as a function of

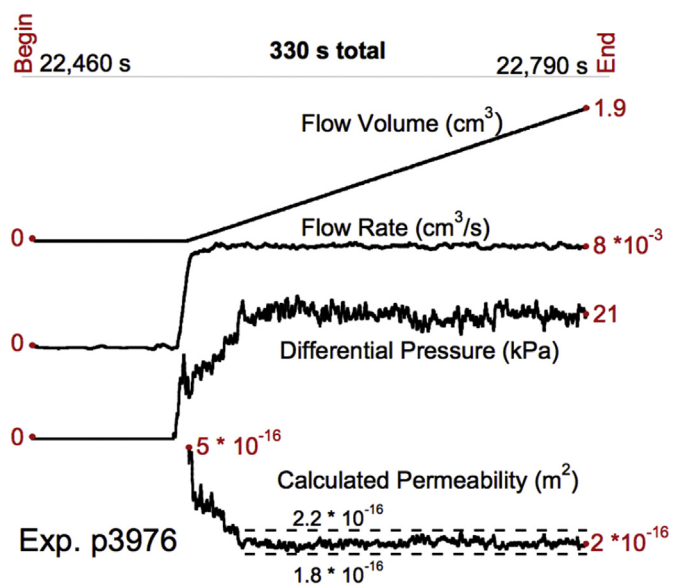


**Fig. 5.** Representative permeability test with constant flow rate. During each  $k$  test a constant flow rate was applied at  $P_{pB}$ , driving a differential pressure between  $P_{pA}$  and  $P_{pB}$ . We measure permeability once flow reaches steady-state, with uncertainty given by noise and small fluctuations in differential pressure.

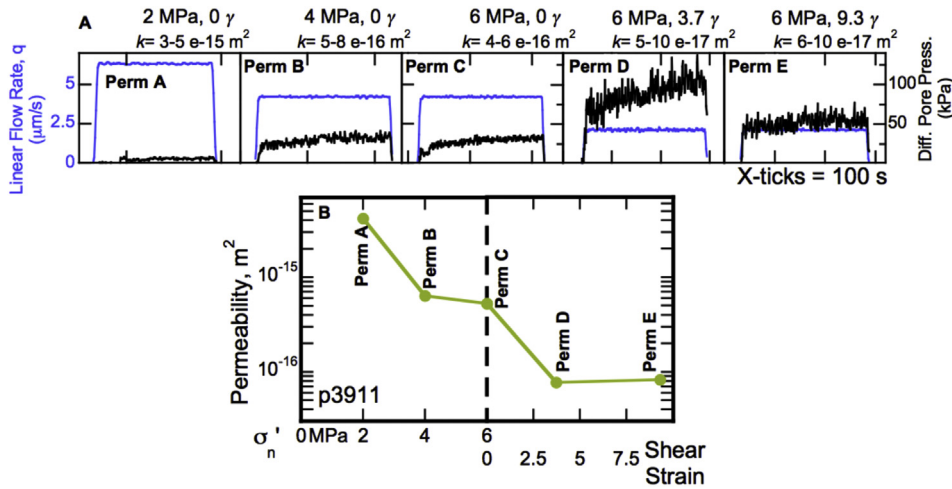


**Fig. 6.** Details of each permeability test from one experiment, p3911 (See Fig. 4). Panel A shows the linear flow rate,  $q = Q/A$ , and resultant differential pore pressure for each  $k$  test. With increasing load and shear strain, we decreased  $q$  to limit  $\Delta P$ , as  $k$  tended to decrease with each step. Low flow rates were also used to limit halite dissolution and momentum transfer effects between fluid and grains. Panel B shows the change in permeability as a function of load (left side) and shear strain (right side), highlighting the tendency for  $k$  to decrease with load and strain.

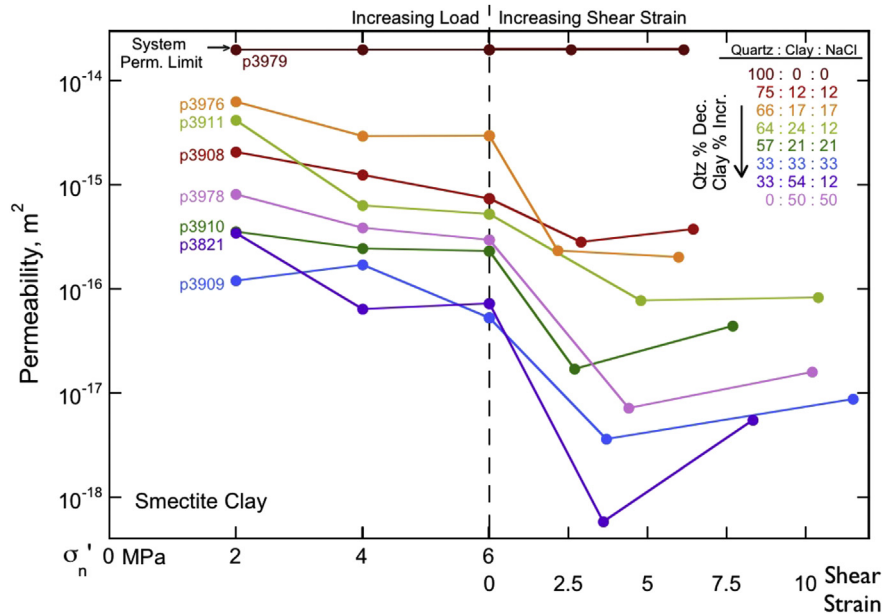
increasing normal stress and shear strain (Figs. 6–8). With increasing normal load from 2 to 6 MPa, all materials experienced a permeability reduction of 0–1 orders of magnitude. Similarly, the application of shear strain (from 0 to 2–5  $\gamma$ ) caused a permeability reduction of 0–2 orders of magnitude. At higher strains however (5–10  $\gamma$ ), some samples exhibited permeability increases of up to 1 order of magnitude (Figs. 7–8).

Fig. 10 shows permeability change with load and strain as a function of quartz content and matrix composition (clay: halite ratio). With increasing effective stress, the observed drop in permeability was generally insensitive to quartz content, matrix composition (clay/halite ranging from 5/95% to 81/19%), and clay type. With initial shear strain, smectite experiments experienced

more  $k$  reduction than illite (Fig. 10B' vs. 10B, respectively), and this  $k$  reduction was enhanced by decreasing quartz content. For example, permeability decreased ~1–2 orders of magnitude with <50% quartz content and only ~0–1 orders of magnitude for higher quartz contents (Fig. 10B').

With the progression from low to high strain, permeability tended to increase. The greatest  $k$  increase occurred for mixtures with high matrix content. Smectite bearing mixtures exhibited the greatest  $k$  increase from low to high strain (Fig. 10C'), perhaps in response to the large  $k$  decrease that occurred with initial strain (Fig. 10B').

To study the role of quartz in determining permeability changes, we compared six experiments with varied quartz content but equal



**Fig. 7.** Permeability as a function of load (left side) and strain (right side) across for montmorillonite experiments. In general,  $k$  increased with high quartz content, and baseline permeabilities spanned ~2 orders of magnitude, OM. For 100% quartz, p3979, we measured very high  $k$ , exceeding the system measurement limit ( $k \sim 2 \times 10^{-14} \text{ m}^2$ ). Across all experiments  $k$  decreased 0–1 OM with increasing load. Similarly,  $k$  decreased by 0–2 OM with increasing strain and the reduction was higher for samples with higher clay content. At higher strains however,  $k$  tended to level out or increase slightly, as was typically the case for high matrix content experiments at very high strains ( $\gamma > 8$ ).

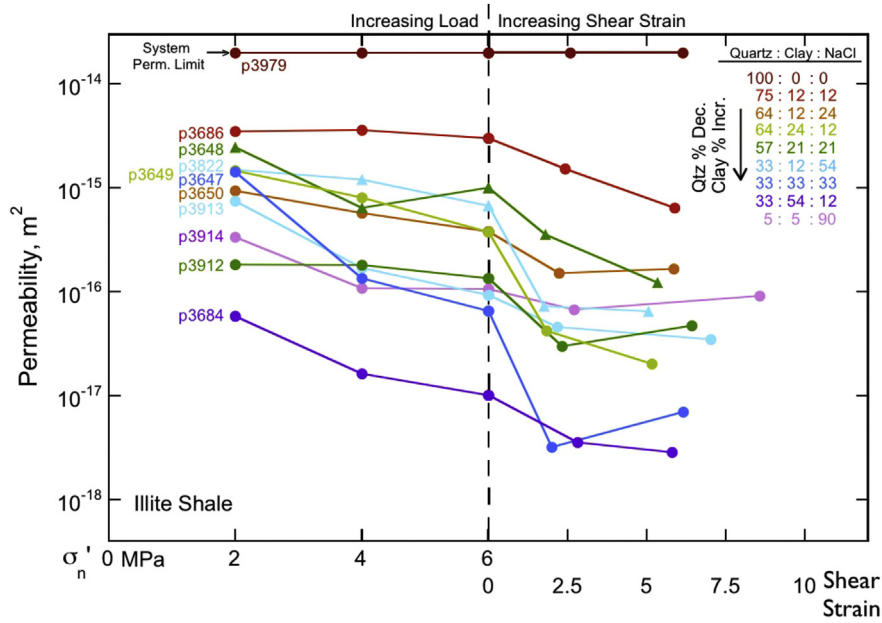


**Fig. 8.** Permeability as a function of load and strain for illite shale experiments. Permeability increased with increasing quartz content, with baseline permeabilities spanning ~2.5 OM.  $k$  decreased with increasing load by 0–1 OM.  $k$  decreased by 0–2 OM as shear strain increased from 0 to ~3; the effect was greater for the samples with the highest clay content.  $k$  did not change dramatically at higher shear strains, and tended to increase in matrix-rich experiments at higher strains ( $\gamma > 6$ ).

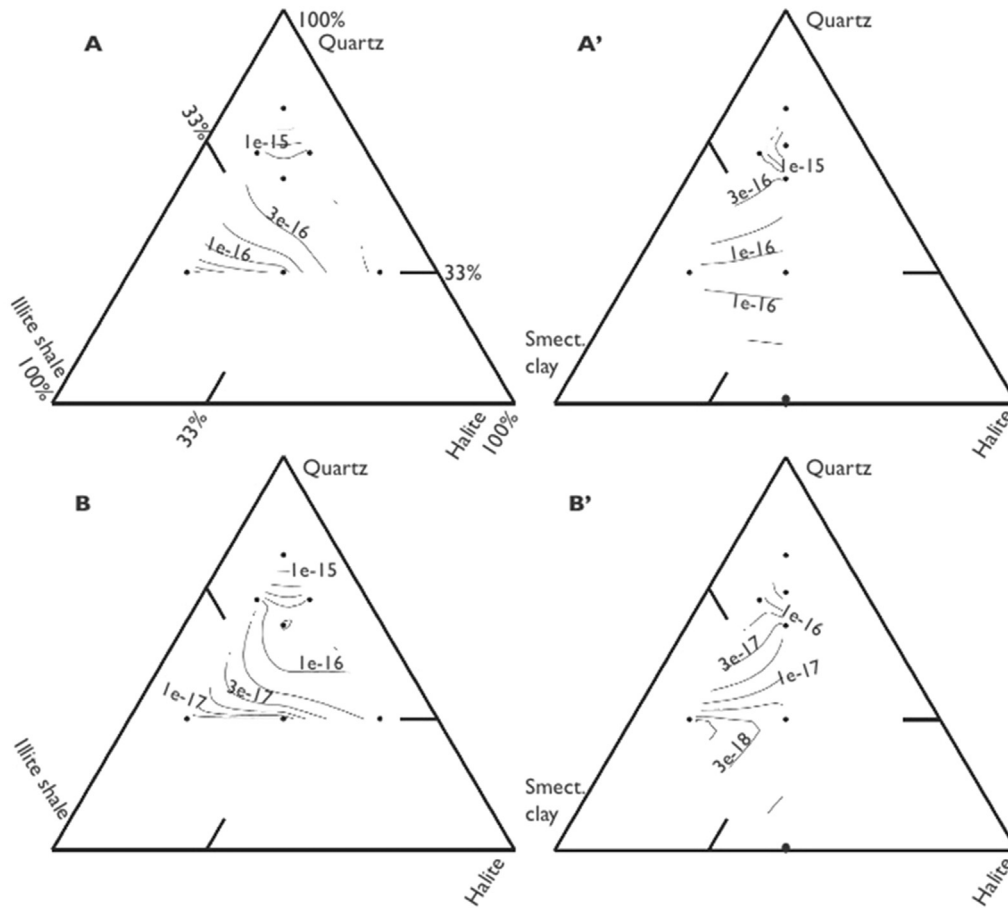


**Fig. 9.** Permeability as a function of mixture composition with contours drawn via interpolation between most experiments. Illite clay samples on left panels, smectite clay on right panels. All data are for 6 MPa effective normal stress. Panels A and A' show data for strain = 0. Panels B and B' show data for low strain (see Figs. 7 and 8). Permeability decreased with increasing clay content.  $k$  was lower for samples with halite relative to quartz at constant clay content. Note that permeability does not show systematic differences between the illite and smectite clay experiments.

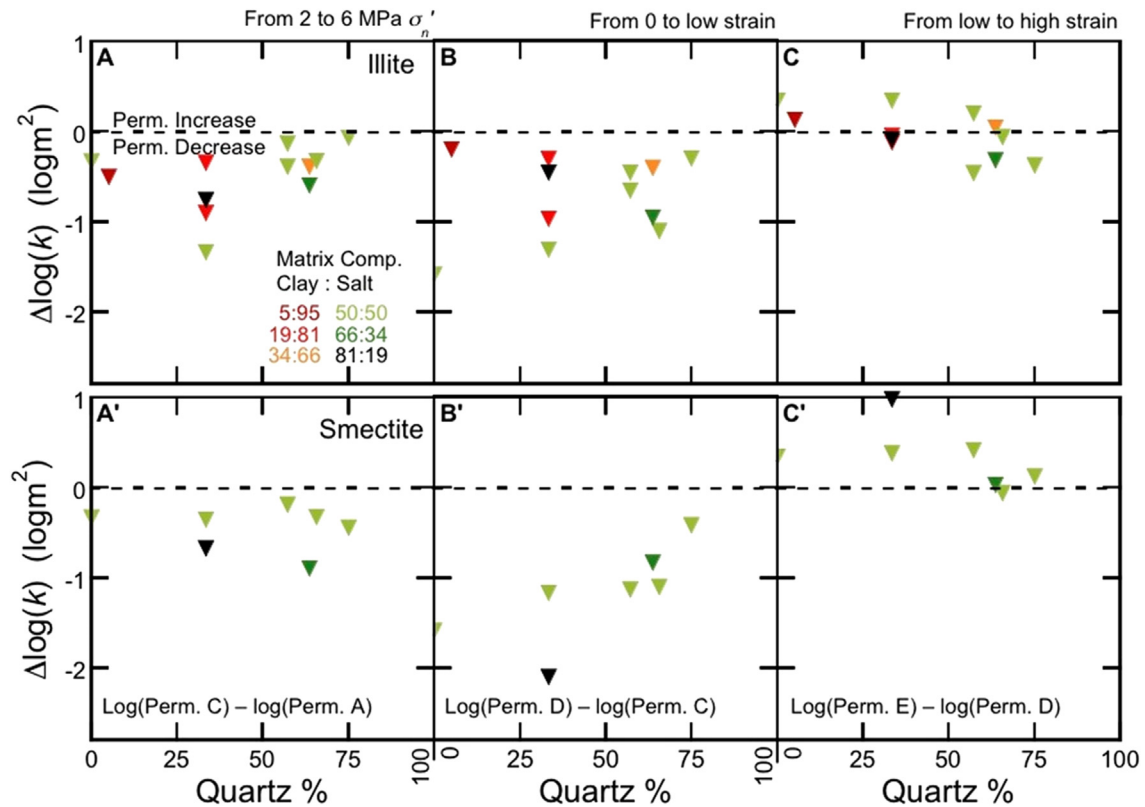


**Fig. 10.** Trends of permeability loss as a function of load (A and A'), low strain (B and B'), and high strain (C and C') for illite and smectite samples, respectively. Colors denote matrix composition (See Fig. 1). With increased load,  $k$  decreased by 0–1 orders of magnitude, with little dependence on clay type (A vs. A'), quartz content, or matrix composition. At low strain, permeability decreased by 0–2 OM, with the strongest change occurring for clay-rich experiments. At higher strain,  $k$  changed little, with the strongest increases occurring for experiments with the highest final strains (see Table 1) and clay contents. (For interpretation of the references to colour in this figure legend, the reader is referred to the web version of this article.)

parts clay and halite (Fig. 11 inset). Fig. 11B and C highlight  $k$  as a function of quartz content at different loads and strains, respectively. At the highest loads (6 MPa  $\sigma_n'$ ), permeability was lowest for 33% quartz ( $\sim 5 \times 10^{-17} \text{ m}^2$ ), and highest for 100% quartz ( $> 2 \times 10^{-14} \text{ m}^2$ ). The fault zone with no quartz exhibited slightly higher permeability than that with 33% quartz. Across these experiments,  $k$  decreased by 0–1 orders of magnitude with increased quartz content (Fig. 11B).

With shear strain, similar to the affect of load, permeability was lowest for the mixture with 33% quartz, 33% smectite, and 33% halite by mass, and generally increased with quartz content (Fig. 11C). As identified previously, the lowest permeabilities for most of these mixtures occurred after initial shear strain (2–4  $\gamma$ ), followed by slight  $k$  increase with further strain (Fig. 11C).

As with permeability, fault friction is strongly dependent on quartz content. Fault layers dominated by quartz, >57%, exhibit similar frictional strengths, at or above 0.6 coefficient of friction ( $\mu = \tau/\sigma_n'$ ) (Fig. 11A). With higher matrix content ( $\leq 33\%$  quartz), friction never exceeded 0.6 and the fault gouge continuously weakens with strain following an initial peak. Weakening behaviors such as these indicate matrix-dominated sliding, perhaps with fabric formation and clay-particle alignment (Rutter et al., 1986; Logan et al., 1992; Haines et al., 2013).

We used microstructural images to document the evolution of shear fabric with shear strain (Figs. 12–14). Samples were collected for thin sections following the final permeability test, and thus these images document the highest strains attained. Halite particles appear as bright-white, quartz particles are large and gray, and the gray matrix is smectite clay (Fig. 12). For high quartz content the

shear zones are framework grain supported (Fig. 12A–C), but they are matrix supported for lower quartz content (Fig. 12D–E). Fabric generation appears to occur primarily in the matrix-supported gouges. Fig. 13 shows higher magnification views of the micrographs from Fig. 12. Experiments with higher quartz contents do not develop a strong matrix fabric (Fig. 13A–C, C'), but fabric is well developed with high matrix content (Fig. 13D–E). Most pore space, especially along quartz grain boundaries, is open as a result of smectite dehydration and densification following each experiment. However, some of this pore space was likely open while the sample was hydrated and intact. In many of these experiment (e.g., p3976) halite grains appear to be in brittle contact with other halite or quartz grains. This allows for accumulation of clay particles between halite grains, potentially leaving pore-space between quartz grains. Halite pressure solution welding is evident throughout these micrographs and in some cases the halite appears to flow with the clay fabric (Fig. 13). For smectite dominated layers, we observe that halite welds with other grains and is in brittle contact with some quartz grains (Fig. 14). In these cases, P-shears developed throughout the layer and halite grains are seen flowing within the clay fabric (Fig. 14).

We conducted permeability tests after the sample had compacted. As such, halite may have acted as a matrix material during these tests, infilling pore space via pressure solution. In some cases, halite grains mix with clay particles to form localized shear zones. Micrographs also indicate halite grains in stress shadows of clast networks and force chains (Fig. 13). This indicates that halite is not simply a 'matrix' material that flows to fill pore space, but rather it can remain in stress shadows and deform brittly, both of which

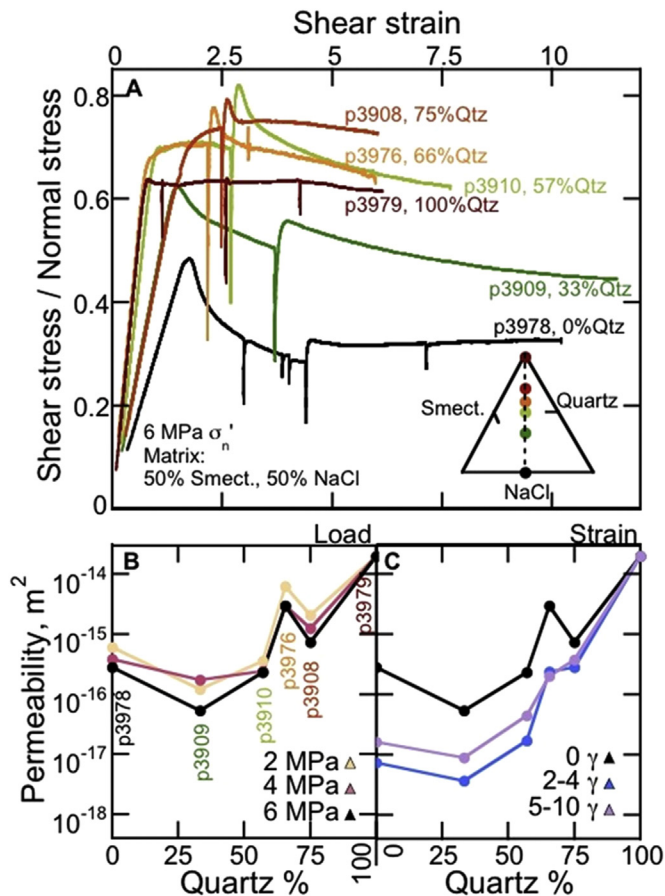


**Fig. 11.** Fault properties as a function of quartz content, with constant clay to halite ratio (see inset in panel A). Sample strength evolves from low to high as quartz content increases (A). In particular, matrix dominated materials weaken dramatically with shear strain, likely resulting from fabric development (Haines et al., 2013), and quartz dominated materials maintain friction values above 0.6. Quartz dominated materials with some matrix exhibit more healing, likely resulting from the halite content, and generally higher stresses, resulting from pore-space infilling (Kaproth et al., 2010). Panels B and C show the permeability evolution with quartz content during these experiments as a function of load and strain, respectively. In general, increased quartz content results in increased  $k$ , with an apparently smooth trend from 100% to 33% quartz. Permeability appears to increase slightly from 33% to 0% quartz. Experiment p3976 is slightly off trend with the other experiments, but after small strain comes into line with other experiments, indicating the effects of shear fabric development during the run-in period.

tend to result in higher pore space than suggested by some previous models (e.g., Revil et al., 2002).

#### 4. Discussion

We find that permeability and frictional strength are strongly sensitive to clay content and shear strain. Faults with small concentrations of clay have dramatically lower  $k$  values than those that do not (Fig. 11). Overall our permeability values range from a minimum of  $5 \times 10^{-19} \text{ m}^2$  to the upper bound that we can measure accurately, which is  $2 \times 10^{-14} \text{ m}^2$ . This included a range of strains and loads for quartz/clay/halite end-member mixtures of 100/0/0%, 33/54/12%, and 5/5/90%, respectively. These values are consistent with previously reported values for pure quartz, illite, montmorillonite-smectite, halite, and mixed granular materials (Peach and Spiers, 1996; Zhang and Tullis, 1998; Crawford et al., 2008; Ikari et al., 2009a; Niemeijer et al., 2008, 2010). For example, Ikari et al., 2009a,b reported  $2 \times 10^{-16} \text{ m}^2$  permeability

for a 50% quartz, 50% montmorillonite mixture ( $\sigma_n' = 12 \text{ MPa}$ ), compared to our value of  $8 \times 10^{-17} \text{ m}^2$  for a similar mixture.

With increased effective stress from 2 to 6 MPa, we observe up to 1 order of magnitude permeability reduction across all of our materials (Figs. 7, 8 and 10). Previous studies show similar magnitudes of  $k$  reduction, especially at such low normal loads, where anelastic compaction is dominant (Faulkner and Rutter, 2003; Crawford et al., 2008; Ikari et al., 2009a).

With shear, fault permeability decreased by up to 2 orders of magnitude and tended to be enhanced in clay-rich materials (Figs. 7, 8, 10 and 11). These changes are in general agreement with previous laboratory works on synthetic fault zones (Zhang and Tullis, 1998; Crawford et al., 2008; Ikari et al., 2009a). Shear driven compaction, fabric formation, and abrasional mixing all tend to assist  $k$  reduction with fault development (Faulkner et al., 2010). Abrasional mixing is especially important in nature because it allows commingling of different wall rock materials, mixing clay in with clasts. Similar processes likely occur during our experiments, helping to mix the gouge and modify the shear fabric (e.g., Rathbun and Marone, 2010). These processes are likely the cause of what we see for experiment p3976, which deviates from other runs with load but falls on trend following shear (Fig. 11).

Shear fabric formation is particularly evident as a function of shear strain for the clay rich fault zones (Figs. 12–14). Friction values for higher quartz content fault zones indicate frictional sliding amongst clasts. In particular, frictional sliding with only 57% quartz indicates that halite is participating in clast-type deformation during shear, as brittle deformation of halite may be operative at these load (6 MPa  $\sigma_n'$ ) and strain-rate (10  $\mu\text{m/s}$ ) conditions (Shimamoto, 1986). The highest frictional strengths occur with some matrix content (e.g., 57–75% quartz), indicating that material in the pore space can obstruct efficient frictional deformation (Kaproth et al., 2010). Peak stress values following holds are likely large resulting from frictional healing via pressure solution of halite (e.g., Marone, 1998; Bos et al., 2000b; Niemeijer et al., 2008, 2010; Carpenter et al., 2016). These peaks may also indicate that the framework clasts are in direct contact with one another, since clay veneer tends to limit fault healing (Dewers and Ortoleva, 1991; Bos et al., 2000a).

Halite appears to have multiple roles in affecting the permeability and mechanical properties of the fault zones. It deforms via ductile deformation and pressure-solution (e.g., Bos et al., 2000b) and also via cracking and other brittle mechanisms. Halite grains appear to participate in force chains (e.g., Fig. 13C') that carry stress in clast-supported materials during shear (Daniels and Hayman, 2008), suggesting brittle failure. However, halite also shows characteristics of ductile flow, as indicated by grain textures and boundary welding, which is presumably a result of pressure solution (e.g., Fig. 13E) (Rutter, 1983; Bos et al., 2000b; Niemeijer et al., 2008).

Throughout our experiments halite particles show characteristics of both brittle and ductile deformation. Some halite grains appear to participate in force chains, which carry stress in a clast-supported gouge (e.g., Daniels and Hayman, 2008) and show some evidence of grain cracking. However, halite grains also show evidence of ductile deformation, such as bending around quartz and halite clasts, and pressure solution. In particular, Fig. 14 shows halite grains welded to quartz particles and clay fabric, evidence for pressure solution (e.g., Bos et al., 2000b). We suspect that some halite grains deform brittly during shear, resulting in clast supported frictional behavior with low quartz concentrations (e.g., 33% quartz; Fig. 11). However, ductile deformation and pressure solution likely dominate halite deformation during holds. Similar ductile processes may occur for halite grains sitting in stress shadows during shear.

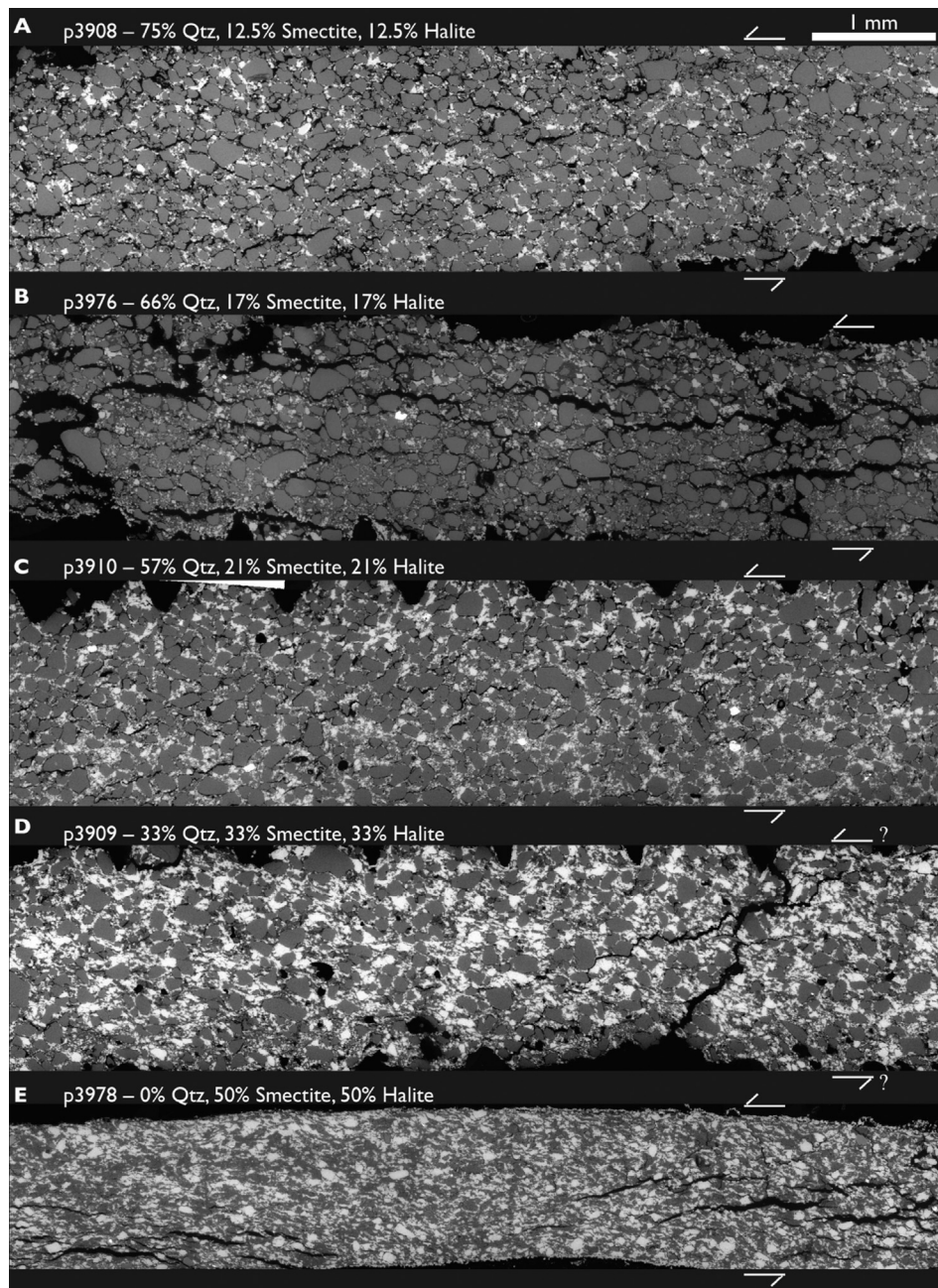


**Fig. 12.** SEM micrographs from five experiments with varied quartz content and constant halite to clay ratio (e.g., Fig. 11). Each of these thin sections was made following the final permeability test, and are thus at high strain (Table 1). Halite particles are bright-white, quartz particles are large and gray, and the gray matrix is smectite clay (individual particles are not visible, at  $<1 \mu\text{m}$  diameter). At high quartz content the faults are framework grain supported (A–C), but are matrix supported at lower quartz content (D–E). Fabric generation appears to only occur in the matrix-supported gouges. Although salt acts as matrix during holds, during shear it appears to be load-bearing, acting as part of the grain-framework skeleton. In particular, p3910 shows halite grains apparently within force chains with quartz grains. Since these thin sections were made following the final hold, salt grains show strong evidence plastic and pressure solution behavior, which are highlighted in Fig. 13.

Although halite acts as matrix during permeability tests, it appears that relicts of shear-driven brittle deformation are maintained during holds and  $k$  tests. The parametric analysis (Fig. 11) indicates that  $k$  was lowest for the mixture with 33% quartz, 33% halite, and 33% smectite by mass, or 28% quartz and 72% matrix by volume, whereas previous models suggest that  $k$  should be lowest with 25–40 vol % matrix (Revil et al., 2002; Crawford et al., 2008). Additionally, SEM micrographs show halite grains involved in force chains (Fig. 13). These observations indicate that halite does not simply participate as matrix. This suggests that minimum porosity and perhaps minimum  $k$  occurs with some higher clay content,

making up for the non-ideal distribution of halite grains.

In experiments with small amounts of quartz (e.g., p3909), the material behaves as if it were matrix dominated regardless of halite content. Fig. 13D shows that p3909 develops fabric within the matrix, with clay and halite aligning in the P orientation. This material also weakened significantly during shear (Fig. 11A), highlighting the role of shear fabric generation. In this case, fluid flow is primarily through the matrix where it is partially retarded by impermeable quartz grains. We suspect that  $k$  might be lower with a slightly higher clast concentration, at the threshold between a matrix and clast supported gouge (Revil et al., 2002). Additionally,

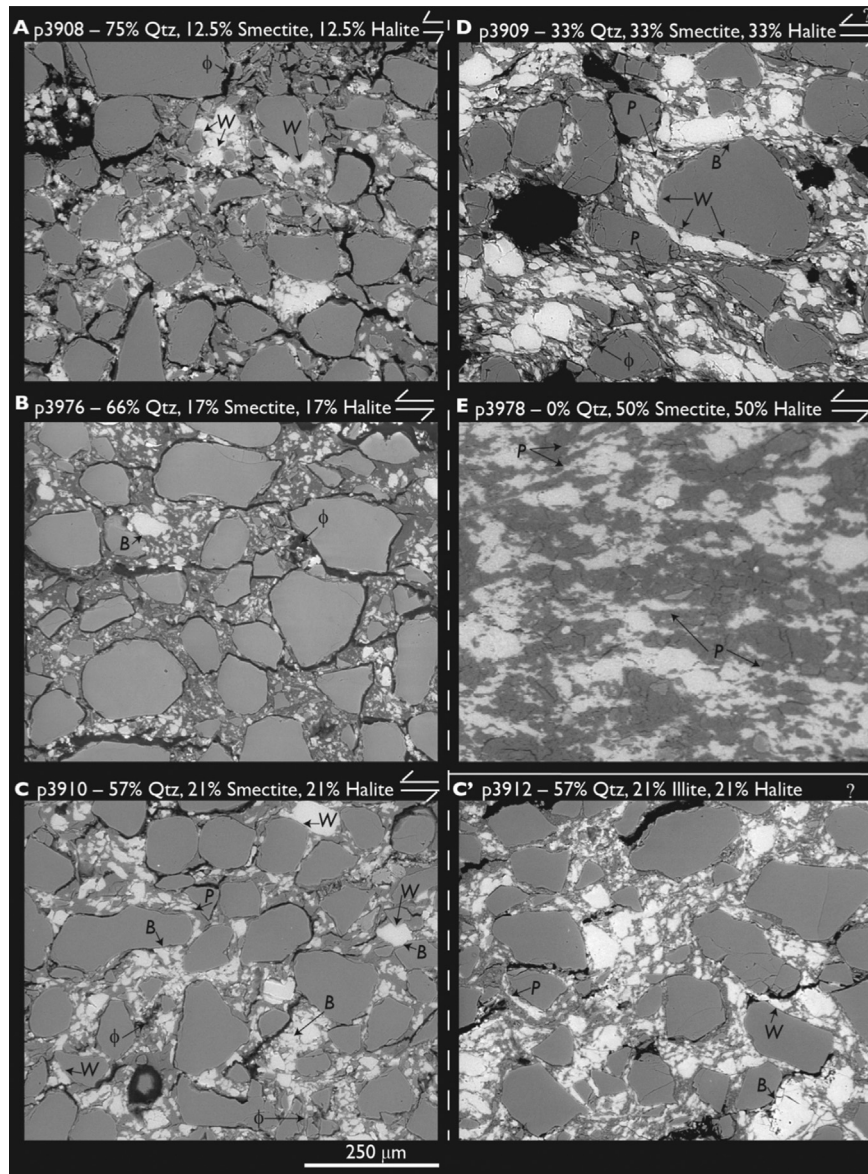


**Fig. 13.** Higher magnification SEM micrographs from Fig. 12. High quartz experiments do not develop a strong matrix fabric (A–C, C'), but fabric is well developed with high matrix content (D–E). Most pore space, especially along quartz grain boundaries, is open as a result of smectite dehydration and densification following each experiment. However some of this pore space was likely open while the sample was hydrated and intact. In many of these experiment (e.g., p3976) halite grains appear to be in brittle contact with other halite or quartz grains, indicated by *B*. This allows for accumulation of clay particles between halite grains, potentially leaving pore-space between quartz grains, indicated by  $\phi$ . Halite welding (via pressure solution) is evident throughout these micrographs, annotated as *W*, and in some cases the halite appears to flow with the clay fabric, noted as *P*. Panels C and F highlight sister experiments with similar mixture ratios, but contain smectite (montmorillonite) clay and illite shale, respectively. These mixtures are similar, but the matrix appears more granular with illite than smectite, owing to the contrast in particle size and some quartz content of the illite shale.

we expect that for a given concentration of clay  $k$  will be preferentially lower with halite over quartz because halite can infill some neighboring pore space via pressure solution (Dewers and Ortoleva, 1991; Niemeijer et al., 2008) and ductile deformation. This may be especially true during times of low shear strain, when halite can flow to occupy porosity between quartz grains and clay fabric. The effect of pressure solution may also be enhanced during holds by the presence of clay particles, which tends to increase diffusion rates (Dewers and Ortoleva, 1991; Renard et al., 2001).

#### 4.1. Application in reservoir settings and implications for faults

While the type of mixed-mode deformation that occurs in our laboratory samples may be relevant for faults that slip seismically

or for faults with low  $\sigma_n'$  (Shimamoto, 1986; Davison, 2009), the application of these data to faults in reservoir rocks is less clear. Several factors may promote aseismic fault creep, such as slower loading rates, higher effective stresses, or higher temperatures. Under these conditions halite may accommodate fault slip dominantly via ductile deformation and pressure solution. Without brittle deformation, halite would behave as a matrix material and, based on previous work, minimum porosity should occur from 60 to 75 vol % quartz (Revil et al., 2002). In this case permeability would likely be lowest for near-pure mixtures of halite and clay, since these mixtures develop mylonitic fabric (Bos et al., 2000a) and halite grains are nearly impermeable (Peach and Spiers, 1996).

In our matrix supported fault zone materials, non-mylonitic fabric is generated within the matrix material, which may have

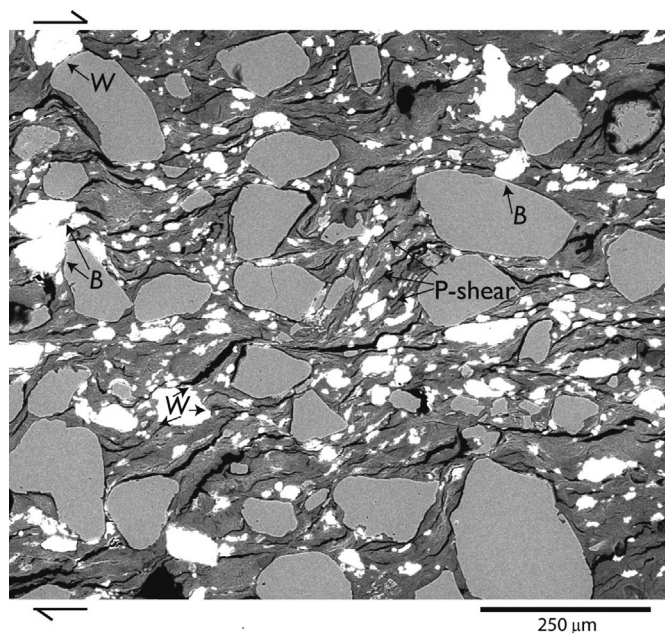


**Fig. 14.** SEM micrograph from smectite dominated experiment, p3821 (54% smectite, 33% quartz, 12% halite). Like the other experiments, halite welds with other grains (W) and is in brittle contact with some quartz grains (B). P-shears developed throughout this material, typical of clay-rich materials. Additionally, halite grains flow with and weld to the clay fabric, and apparently do not locally disrupt the clay fabric, unlike quartz grains.

implications for fault permeability decrease at low strain and increase at higher strains. Fabric generation appears to be enhanced with greater clay content (Fig. 13D vs. Fig. 13B), and generally aligns clay particles into the P-orientation or the fault parallel Y or B orientation (e.g., Haines et al., 2013). Fault parallel clays may retard across-fault flow, the direction tested here, perhaps reducing permeability by an order of magnitude in that direction (Faulkner et al., 2010). With greater shear however, macro-fabric features (e.g., Riedel, P, and Y shears) are developed (Fig. 14) (Logan et al., 1992; Haines et al., 2009, 2013), and fluid flow may be enhanced along these features (Arch and Maltman, 1990; Zhang and Tullis, 1998; Zhang et al., 1999). This may be especially true along high angle P-shears, which readily develop in high clay content experiments (Fig. 14). Thus  $k$  may increase in clay rich fault gouge from low to high strain (Fig. 10), similar to observations by Crawford et al., (2008). Previous studies at higher loads show continued  $k$  decrease with strain, likely owing to the effects of comminution and compaction (Ikari et al., 2009a; Faulkner et al., 2010), which was limited in our low-stress, quartz-rich system (e.g., note the intact grains visible after shear in Fig. 13). Finally, we note that our experiments, with halite saturated brine, apply to faults in halite bearing units where fluid flow rates are slow compared to the rate of dissolution. Moreover, the observation that permeability responses are similar between the illite and smectite bearing lithologies suggests that halite may prevent swelling of the smectite grains.

## 5. Conclusions

Our experiments were designed to investigate the permeability evolution of marine sediment faults with intermixed halite and clay. We found that fault permeability has strong dependence on clay content, reducing  $k$  by up to two orders of magnitude under otherwise identical conditions. For permeability we found that halite and quartz are generally interchangeable, with slightly

enhanced  $k$  reduction with halite resulting from enhanced compaction during holds. We studied loading conditions analogous to those of the seismic cycle, with periods of relatively fast slip followed by periods of quiescence. Halite grains show evidence for both brittle and ductile deformation, behaving brittly during shear and ductily during hold periods. We found that halite cannot be considered matrix when making minimum porosity estimates of a mixture; minimum porosity will occur instead with a greater proportion of fine particles.

For all compositions of marine sediment faults tested here we found that permeability was greatly reduced with small shear strain ( $\gamma < 5$ ), up to two orders of magnitude. Greater strain had limited effect on permeability, and occasionally enhanced permeability, presumably due to disruption of flow retarding shear fabric. Similarly, we found that fault permeability decreased by  $<1$  order of magnitude with increased load ( $<6$  MPa  $\sigma_n'$ ). These results are in general agreement with previous works showing the permeability effect of compaction with load and abrasional mixing and clay smearing with shear (Zhang and Tullis, 1998; Faulkner and Rutter, 2001, 2003; Crawford et al., 2008; Ikari et al., 2009a). Our results indicate that permeability of faults in marine sediment is dictated strongly by clay content, and that the most dramatic permeability changes occur with relatively small fault throw. These findings suggest that minor faults, which may be difficult to detect in seismic data, may have dramatic implications for reservoir characterization.

## Acknowledgements

We thank S. Swavelly for help in the laboratory, D. Elsworth for helpful discussions, and A. Billi and an anonymous reviewer for thorough reviews and insightful comments that improved the manuscript. This work is the result of support from the Chevron Energy Technology Company. This support is gratefully acknowledged. All data used in this article are available by contacting the corresponding author.

## References

- Antonellini, M., Aydin, A., 1994. Effect of faulting on fluid flow in porous sandstones: petrophysical properties. *Am. Assoc. Pet. Geol. Bull.* 78, 335–377.
- Arch, J., Maltman, A., 1990. Anisotropic permeability and tortuosity in deformed wet sediments. *J. Geophys. Res.* Solid 95 (89), 9035–9045.
- Aydin, A., 2000. Fractures, faults, and hydrocarbon entrapment, migration and flow. *Mar. Pet. Geol.* 17, 797–814.
- Aydin, A., Johnson, A.M., 1983. Analysis of faulting in porous sandstones. *J. Struct. Geol.* 5.
- Ballas, G., Soliva, R., Sizun, J.P., Benedict, A., Cavailhes, T., Raynaud, S., 2012. The importance of the degree of cataclasis in shear bands for fluid flow in porous sandstone, Provence, France. *AAPG Bull.* 96 (11), 2167–2186.
- Balsamo, F., Storti, F., 2010. Grain size and permeability evolution of soft-sediment extensional sub-seismic and seismic fault zones in high-porosity sediments from the Croton basin, southern Apennines, Italy. *Mar. Pet. Geol.* 27 (4), 822–837.
- Baud, P., Klein, E., Wong, T.F., 2004. Compaction localization in porous sandstones: spatial evolution of damage and acoustic emission activity. *J. Struct. Geol.* 26 (4), 603–624.
- Benson, P., Schubnel, A., Vinciguerra, S., Trovato, C., Meredith, P., Young, R.P., 2006. Modeling the permeability evolution of microcracked rocks from elastic wave velocity inversion at elevated isostatic pressure. *J. Geophys. Res.* 111.
- Bentley, M.R., Barry, J.J., 1991. Representation of Fault Sealing in a Reservoir Simulation: Cormorant Block IV. Society of Petroleum Engineers, UK North Sea. Paper 22667.
- Billi, A., Salvini, F., Storti, F., 2003. The damage zone-fault core transition in carbonate rocks: implications for fault growth, structure and permeability. *J. Struct. Geol.* 25, 1779e1794.
- Bjørlykke, K., Hüg, K., 1997. Effects of burial diagenesis on stress, compaction and fluid flow in sedimentary basins. *Mar. Pet. Geol.* 14, 267–276.
- Bos, B., Spiers, C., 2000. Effect of phyllosilicates on fluid-assisted healing of gouge-bearing faults. *Earth Planet. Sci. Lett.* 184 (1), 199–210.
- Bos, B., Peach, C., Spiers, C., 2000a. Frictional-viscous flow of simulated fault gouge caused by the combined effects of phyllosilicates and pressure solution. *Tectonophysics* 327 (3–4), 173–194.

- Bos, B., Peach, C., Spiers, C., 2000b. Slip behavior of simulated gouge-bearing faults under conditions favoring pressure solution. *J. Geophys. Res.* 105 (B7), 16699.
- Caine, J.S., Forster, C.B., 1999. Fault zone architecture and fluid flow: insights from field data and numerical modeling. In: Haneberg, W.C., et al. (Eds.), *Faults and Subsurface Flow in Shallow Crust: American Geophysical Monograph*, vol. 113, pp. 101–127.
- Caine, J.S., Evans, J.P., Forster, C.B., 1996. Fault zone architecture and permeability structure. *Geology* 24, 1025–1028.
- Carpenter, B.M., Saffer, D.M., Marone, C., 2015. Frictional properties of the active San Andreas Fault at SAFOD: implications for fault strength and slip behavior. *J. Geophys. Res.* 120, 5273–5289. <http://dx.doi.org/10.1002/2015JB011963>.
- Carpenter, B.M., Ikari, M.J., Marone, C., 2016. Laboratory observations of time-dependent frictional strengthening and stress relaxation in natural and synthetic fault gouges. *J. Geophys. Res.* 121, 1183–1201. <http://dx.doi.org/10.1002/2015JB012136>.
- Carruthers, D., Cartwright, J., Jackson, M.P.A., Schutjens, P., 2013. Origin and timing of layer-bound radial faulting around North Sea salt stocks: new insights into the evolving stress state around rising diapirs. *Mar. Pet. Geol.* 48, 130e148.
- Cheung, C.S., Baud, P., Wong, T. F., 2012. Effect of grain size distribution on the development of compaction localization in porous sandstone. *Geophys. Res. Lett.* 39 (21).
- Chuhan, F.A., Kjeldstad, A., Bjorlykke, K., Hoeg, K., 2003. Experimental compression of loose sands: relevance to porosity reduction during burial in sedimentary basins. *Can. Geotech. J.* 40 (5), 995–1011.
- Crawford, B.R., 1998. Experimental fault sealing: shear band permeability dependency on cataclastic fault gouge characteristics. In: Coward, M.P., Daltaban, T.S., Johnson, H. (Eds.), *Structural Geology in Reservoir Characterisation*, vol. 127, pp. 27–48. Special Publication of the Geological Society of London.
- Crawford, B.R., Faulkner, D.R., Rutter, E.H., 2008. Strength, porosity, and permeability development during hydrostatic and shear loading of synthetic quartz-clay fault gouge. *J. Geophys. Res.* 113.
- Daniel, R.F., Kaldi, J.G., 2008. Evaluating seal capacity of caprocks and intraformational barriers for the sequestration of CO<sub>2</sub>. In: PESA Eastern Australian Basins Symposium III, pp. 475–484.
- Daniels, K.E., Hayman, N.W., 2008. Force chains in seismogenic faults visualized with photoelastic granular shear experiments. *J. Geophys. Res.* 113.
- Davison, I., 2009. Faulting and fluid flow through salt. *J. Geol. Soc.* 166, 205–216. <http://dx.doi.org/10.1144/001676492008-064>.
- De Paola, N., Faulkner, D.R., Collettini, C., 2009. Brittle versus ductile deformation as the main control on the transport properties of low-porosity anhydrite rocks. *J. Geophys. Res.* 114.
- Dewers, T., Ortoleva, P., 1991. Influences of clay minerals on sand-stone cementation and pressure solution. *Geology* 19, 1045–1048.
- Evans, J.P., Forster, C.B., Goddard, J.V., 1997. Permeability of fault-related rocks, and implications for hydraulic structure of fault zones. *J. Struct. Geol.* 19 (11), 1393–1404.
- Faoro, I., Elsworth, D., Marone, C., 2012. Permeability evolution during dynamic stressing of dual permeability media. *J. Geophys. Res.* 117, No. B1, B01310.
- Faoro, I., Vinciguerra, S., Marone, C., Elsworth, D., Schubnel, A., 2013. Linking permeability to crack density evolution in thermally stressed rocks under cyclic loading. *Geophys. Res. Lett.* 40 <http://dx.doi.org/10.1002/grl.50436>.
- Faulkner, D.R., Rutter, E., 2001. Can the maintenance of overpressured fluids in large strike-slip fault zones explain their apparent weakness. *Geology* 29, 503–506.
- Faulkner, D.R., Rutter, E., 2003. The effect of temperature, the nature of the pore fluid, and subyield differential stress on the permeability of phyllosilicate-rich fault gouge. *J. Geophys. Res.* 108.
- Faulkner, D., Jackson, C., Lunn, R., Schlichte, R., Shipton, Z., Wibberley, C., Withjack, M., 2010. A review of recent developments concerning the structure, mechanics and fluid flow properties of fault zones. *J. Struct. Geol.* 32 (11), 1557–1575.
- Fisher, Q.J., Harris, S.D., McAllister, E., Knipe, R.J., Bolton, A.J., 2001. Hydrocarbon flow across sealing faults: theoretical constraints. *Mar. Pet. Geol.* 18, 251–257.
- Fisher, Q.J., Knipe, R.J., 1998. Fault sealing processes in siliciclastic sediments. In: Geological Society, London, Special Publications, vol. 147, p. 117e134.
- Fisher, Q.J., Knipe, R.J., 2001. The permeability of faults within siliciclastic petroleum reservoirs of the North Sea and Norwegian Continental Shelf. *Mar. Pet. Geol.* 18, 1063e1081.
- Foroozan, R., Elsworth, D., Flemings, P., Bilotti, F., Muhuri, S., 2012. The role of permeability in fault zones on the structural and hydro-mechanical characteristics of shortening basins. *Mar. Pet. Geol.* 29, 143–152.
- Fort, X., Brun, J.-P., 2012. Kinematics of regional salt flow in the northern Gulf of Mexico. In: Alsop, G.I., Archer, S.G., Hartley, A.J., Grant, N.T., Hodgkinson, R. (Eds.), *Salt Tectonics, Sedimentation and Prospectivity*, vol. 363. Geological Society, London, p. 265e287. Special Publications.
- Fortin, J., Schubnel, A., Gueguen, Y., 2005. Elastic wave velocities and permeability evolution during compaction of Bleurswiller sandstone. *Int. J. Rock Mech. Min. Sci.* 42 (7–8), 873–889.
- Fossen, H., Bale, A., 2007. Deformation bands and their influence on fluid flow. *AAPG Bull.* 91 (12), 1685–1700.
- Gibson, R.G., 1998. Physical character and fluid flow properties of sandstone-derived fault zones. In: Coward, M.P., Daltaban, T.S., Johnson, H. (Eds.), *Structural Geology in Reservoir Characterisation*, vol. 127, pp. 83–98. Special Publication of the Geological Society of London.
- Gomila, R., Mitchell, T.M., Arancibia, G., Combrano, J.M., Faulkner, D.R., 2016. Palaeopermeability structure within fault zones: a snap-shot from microfracture analyses in a strike-slip system. *J. Struct. Geol.* 83, 103–120.
- Haines, S.H., van der Pluijm, B. a., Ikari, M.J., Saffer, D.M., Marone, C., 2009. Clay fabric intensity in natural and artificial fault gouges: implications for brittle fault zone processes and sedimentary basin clay fabric evolution. *J. Geophys. Res.* 114.
- Haines, S.H., Kaproth, B.M., Marone, C., Saffer, D., van der Pluijm, B. a., 2013. Shear zones in clay-rich fault gouge: a laboratory study of fabric element development and evolution. *J. Struct. Geol.* 114 (B5).
- Harding, R., Huuse, M., 2015. Salt on the move: multi stage evolution of salt diapirs in The Netherlands North Sea. *Mar. Pet. Geol.* 61, 39e55.
- Hudec, M.R., Jackson, M.P.A., 2007. Terra infirma: understanding salt tectonics. *Earth Sci. Rev.* 82, 1–28.
- Ikari, M.J., Saffer, D.M., 2012. Permeability contrasts between sheared and normally consolidated sediments in the Nankai accretionary prism. *Mar. Geol.* 295–298, 1–13. <http://dx.doi.org/10.1016/j.margeo.2011.11.006>.
- Ikari, M., Saffer, D., Marone, C., 2009a. Frictional and hydrologic properties of clay-rich fault gouge. *J. Geophys. Res.* 114 (B5), B05409.
- Ikari, M.J., Saffer, D.M., Marone, C., 2009b. Frictional and hydrologic properties of a major spray fault system, Nankai subduction zone. *Geophys. Res. Lett.* 36 (20), L20313.
- Ishibashi, T., McGuire, T., Tsuchiya, N., Elsworth, D., 2012. Permeability evolution of carbonate fractures: competition between stress and reactivity. *Water Resour. Res.* 48 (7).
- Jackson, M.P.A., Vendeville, B.C., Schultz-Ela, D.D., 1994. Structural dynamics of salt systems. *Annu. Rev. Earth Planet. Sci.* 22, 93–117.
- Kaproth, B.M., Cashman, S.M., Marone, C., 2010. Deformation band formation and strength evolution in un lithified sand: the role of grain breakage. *J. Geophys. Res.* 115, B12103.
- Kaproth, B.M., Marone, C., 2014. Evolution of elastic wave speed during shear-induced damage and healing within laboratory fault zones. *J. Geophys. Res.* 119.
- Kim, Y.-S., Peacock, D.C.P., Sanderson, D.J., 2004. Fault damage zones. *J. Struct. Geol.* 26, 503–517.
- Knipe, R.J., 1992. Faulting processes and fault seal. In: Larsen, R.M., Brekke, B.T., Talleras, E. (Eds.), *Structural and Tectonic Modelling and its Application to Petroleum Geology*, vol. 1, pp. 325–342. NPF Special Publication.
- Logan, J., Dengo, C., Higgs, N., Wang, Z.-Z., 1992. Fabrics of experimental fault zones: their development and relationship to mechanical behavior. In: *Fault Mechanics and Transport Properties of Rocks*. Academic Press, pp. 33–67.
- López, D., Smith, L., 1995. Fluid flow in fault zones: analysis of the interplay of convective circulation and topographically driven groundwater flow. *Water Resour. Res.* 31 (6), 1489–1503.
- Lothe, A.E., Gabrielsen, R.H., Hagen, N.B., Larsen, B.T., 2002. An experimental study of the texture of deformation bands: effects on the porosity and permeability of sandstones. *Pet. Geosci.* 8 (3), 195–207.
- Marone, C., 1998. Laboratory-derived friction laws and their application to seismic faulting. *Ann. Rev. Earth Plan. Sci.* 26, 643–696.
- Mitchell, T.M., Faulkner, D.R., 2008. Experimental measurements of permeability evolution during triaxial compression of initially intact crystalline rocks and implications for fluid flow in fault zones. *J. Geophys. Res.* 113.
- Mitchell, T.M., Faulkner, D.R., 2012. Towards quantifying the matrix permeability of fault damage zones in low porosity rocks. *Earth Planet. Sci. Lett.* 339–340, 24–31.
- Mondol, N.H., Bjorlykke, K., Jahren, J., 2008. Experimental compaction of clays: relationship between permeability and petrophysical properties in mudstones. *Pet. Geosci.* 14 (4), 319–337.
- Niemeijer, A., Marone, C., Elsworth, D., 2008. Healing of simulated fault gouges aided by pressure solution: results from rock analogue experiments. *J. Geophys. Res. Solid Earth* 113 (B4), B04204.
- Niemeijer, A., Marone, C., Elsworth, D., 2010. Frictional strength and strain weakening in simulated fault gouge: competition between geometrical weakening and chemical strengthening. *J. Geophys. Res.* 115 (B10), B10207.
- Odling, N.E., Harris, S.D., Knipe, R.J., 2004. Permeability scaling properties of fault damage zones in siliciclastic rocks. *J. Struct. Geol.* 26.
- Olierook, H.K.H., Timms, N.E., Hamilton, P.J., 2014. Mechanisms for permeability modification in the damage zone of a normal fault, northern Perth Basin, Western Australia. *Mar. Pet. Geol.* 50, 130e147.
- Peach, C.J., Spiers, C.J., 1996. Influence of crystal plastic deformation on dilatancy and permeability development in synthetic salt rock. *Tectonophysics* 256 (1–4), 101–128.
- Rathbun, A.P., Marone, C., 2010. Effect of strain localization on frictional behavior of sheared granular materials. *J. Geophys. Res.* 115, B01204. <http://dx.doi.org/10.1029/2009JB006466>.
- Renard, F., Dysthe, D., Feder, J., 2001. Enhanced pressure solution creep rates induced by clay particles: experimental evidence in salt aggregates. *Geophys. Res. Lett.* 28 (7), 1295–1298.
- Revil, A., Grauls, D., Brévert, O., 2002. Mechanical compaction of sand/clay mixtures. *J. Geophys. Res.* 107 (B11), 2293. <http://dx.doi.org/10.1029/2001JB000318>.
- Rowan, M., Jackson, M., Trudgill, B., 1999. Salt-related fault families and fault welds in the northern gulf of Mexico. *AAPG Bull.* 9 (9), 1454–1484.
- Rutter, E.H., 1983. Pressure solution in nature, theory and experiment. *J. Geol. Soc.* 140 (5), 725–740. <http://dx.doi.org/10.1144/gsjgs.140.5.0725>.
- Rutter, E.H., Maddock, R.H., Hall, S.H., White, S.H., 1986. Comparative microstructures of natural and experimentally produced clay-bearing fault gouges. *PAGEOPH* 124 (1–2), 3–30.
- Samuelson, J., Elsworth, D., Marone, C., 2009. Shear-induced dilatancy of fluid-

- saturated faults: experiment and theory. *J. Geophys. Res.* 114 (B12), B12404.
- Savage, H.M., Brodsky, E.E., 2011. Collateral damage: evolution with displacement of fracture distribution and secondary fault strands in fault damage zones. *J. Geophys. Res.* 116.
- Scuderi, M.M., Kitajima, H., Carpenter, B.M., Saffer, D.M., Marone, C., 2015. Evolution of permeability across the transition from brittle failure to cataclastic flow in porous siltstone. *Geochem. Geophys. Geosys.* 16 <http://dx.doi.org/10.1002/2015GC005932>.
- Seebeck, H., Tenthoery, E., Consoli, c, Nicol, A., 2015. Polygonal faulting and seal integrity in the Bonaparte Basin, Australia. *Mar. Pet. Geol.* 60, 120e135.
- Shimamoto, T., 1986. Transition between frictional slip and ductile flow for halite shear zones at room temperature. *Science* 231 (4739).
- Shipton, Z.K., Evans, J.P., Thompson, L.B., 2005. The geometry and thickness of deformation-band fault core and its influence on sealing characteristics of deformation-band fault zones. In: Sorkhabi, R., Tsuji, Y. (Eds.), *Faults, Fluid Flow, and Petroleum Traps*. AAPG Memoir, vol. 85, pp. 181–195.
- Skurtveit, 2013. *Experimental Investigation of Deformation Mechanisms During Shear-Enhanced Compaction in Poorly Lithified Sandstone and Sand*.
- Smith, D., 1966. Theoretical considerations of sealing and non-sealing faults. AAPG Bull. 50 (2), 363–374.
- Sternlof, K.R., Chapin, J.R., Pollard, D.D., Durlifsky, L.J., 2004. Permeability effects of deformation band arrays in sandstone. AAPG Bull. 88 (9), 1315–1329.
- Takahashi, M., Mizoguchi, K., Kitamura, K., Masuda, K., 2007. Effects of clay content on the frictional strength and fluid transport property of faults. *J. Geophys. Res.* 112 (B8), B08206.
- Tueckmantel, T., Fisher, Q.T., Knipe, R.J., Lickorish, H., Khalil, S.M., 2010. Fault seal prediction of seismic-scale normal faults in porous sandstone: a case study from the eastern Gulf of Suez rift, Egypt. *Mar. Pet. Geol.* 27, 334–350.
- Wibberley, C.A.J., Shimamoto, T., 2003. Internal structure and permeability of major strike-slip fault zones: the median tectonic line in mie prefecture, southwest Japan. *J. Struct. Geol.* 25, 59–78.
- Wong, T.F., Baud, P., 2012. The brittle-ductile transition in porous rock: a review. *J. Struct. Geol.* 44, 25–53.
- Zhang, S., Tullis, T.E., 1998. The effect of fault slip on permeability and permeability anisotropy in quartz gouge. *Tectono.* 295 (1–2), 41–52.
- Zhang, S., Tullis, T.E., Scruggs, V.J., 1999. Permeability anisotropy and pressure dependency of permeability in experimentally sheared gouge materials. *J. Struct. Geol.* 21 (7), 795–806.